The Journal of Chemical Physics ARTICLE scitation.org/journal/jcp

# Visible-light photocatalysis and charge carrier dynamics of elemental crystalline red phosphorus

Cite as: J. Chem. Phys. 153, 024707 (2020); doi: 10.1063/5.0013142
Submitted: 8 May 2020 • Accepted: 22 June 2020 •
Published Online: 10 July 2020



Lin Jing,[1,2] Ruixue Zhu,[3] Yun Hau Ng,[4] Zhuofeng Hu,[1] Wey Yang Teoh,[4] David Lee Phillips,[3,a)] and Jimmy C. Yu[1,b)]

## AFFILIATIONS

[1]Department of Chemistry, The Chinese University of Hong Kong, Shatin, New Territories, Hong Kong, China
[2]College of Environmental and Energy Engineering, Beijing University of Technology, Beijing, China
[3]Department of Chemistry, University of Hong Kong, Pokfulam Road, Hong Kong, China
[4]School of Chemical Engineering, The University of New South Wales, Sydney, NSW 2052, Australia

**Note:** This paper is part of the JCP Special Topic on Photocatalysis and Photoelectrochemistry.
[a)]**Email:** phillips@hku.hk
[b)]**Author to whom correspondence should be addressed:** jimyu@cuhk.edu.hk

## ABSTRACT

Elemental red phosphorus (red P) is a new class of photocatalysts with a desirable bandgap of ~1.7 eV and has a strong visible-light response. Here, we show that the efficiency of red P is limited by severe electron trapping at deep traps that are intrinsic to the different crystal facets of the red P. To overcome this, we synthesized the red P/RGO (reduced graphene oxide) composite in a one-step ampoule chemical vapor deposition synthesis that formed a conducive interface between the red P photocatalyst and the RGO acceptor for efficient interfacial charge transport. As substantiated through photoelectrochemical characterization and ultrafast (femtoseconds) transient absorption spectroscopy, the interfacing with RGO provided a rapid pathway for the photocharges in red P to be interfacially separated, thereby circumventing the slower the charge trapping process. As a result, up to a sevenfold increase in the photocatalytic hydrogen production rate (apparent quantum yield = 3.1% at 650 nm) was obtained for the red P/RGO relative to the pristine red P.



## I. INTRODUCTION

Significant efforts have been made in recent years to develop new photocatalysts based on earth-abundant and non-toxic elements.[1–3] While a wide range of simple and mixed metal oxides (e.g., $TiO_2$, ZnO, $Fe_2O_3$, $SrTiO_3$, and $BiVO_4$) were proven to be photocatalytically active, the highly positive O 2p levels that form the valence band edges of these metal oxides inevitably led to wider bandgaps than the ideal 1.5 eV for optimum solar conversion. In this respect, sulfides-, nitrides-, and phosphides-based photocatalysts are promising alternatives, although the compromised valence band potentials and occasional photo- or aqueous-instability may render them unsuitable for oxygen evolution reaction, i.e., the half reaction of water splitting. As a newly discovered class of photocatalysts, the elemental red phosphorus (red P) possesses a moderate bandgap of ~1.7 eV[4–10] that allows it to be activated deep in the visible spectrum. In fact, the low-cost and environmentally benign red P was shown to exhibit the highest hydrogen evolution rates among elemental photocatalysts, including crystalline Si.[4,5]

The elemental red P exists in a number of different chemical phases and structures, namely, amorphous, Hittorf, fibrous, and tubular.[4,5,11–15] Among these, the amorphous, Hittorf, and fibrous red P were reported to be photocatalytically active.[4,5] However, in comparison with the traditional photocatalysts such as $TiO_2$ or even newer ones such as g-$C_3N_4$, the photocatalytic activity of red P is still limited. As a newly discovered photocatalyst, the bulk of the literature on red P has been focused largely on the synthesis strategies to improve its performance.[13,16–19] Limited work exists on the

investigation of the fundamental photophysical processes, i.e., photocharge transport, trapping, and surface transfer, to elucidate the photoactivity of the red P. Such effort is deemed necessary to pave the way for the rational design of highly active red P.

In this work, we present, for the first time, the investigation of the charge carrier dynamics of red P using ultrafast time-resolved absorption (TA) spectroscopy. The study revealed that the photocatalytic activity of red P is limited by charge trapping on the intrinsic deep trap states (TSs). Unlike the surface (shallow) traps that are often beneficial for catalyzing redox reactions with a relatively long residence time,[20–22] deeply trapped electrons cannot be easily detrapped and, hence, are susceptible to charge recombination. Unless mitigated or circumvented, they result in low photocatalytic activities.[23–27]

As will be shown in the current work, we found that the severe charge trapping in red P can be alleviated by interfacing with an electron acceptor material such as reduced graphene oxide (RGO) sheets. The efficient interfacial charge transport between the red P and RGO minimizes the charge trapping at the TS. This resulted in the red P/RGO composite photocatalyst that shows remarkable visible-light activity in the hydrogen evolution reaction. The new insights into the charge carrier dynamics gained from the current work would be beneficial for further improvement of the photocatalytic activity of the red P or its allotropes.

## II. EXPERIMENTAL SECTION

### A. Materials

Commercial red P, graphite, sulfuric acid ($H_2SO_4$, 98%), potassium permanganate ($KMnO_4$, 99.5%), Methanol, sodium nitrate ($NaNO_3$, 99%), and hydrogen peroxide ($H_2O_2$, 30%) were purchased from Sigma Aldrich. Deionized water was purified using the MilliQ Plus apparatus.

### B. Preparation of crystalline red P and red P/RGO composite

The purification of commercial red P and the preparation of GO are detailed in the supplementary material. A mixture of 90 mg purified red P and 10 mg GO was dispersed in a 50 ml ethanol/water solution. The suspension was sonicated for 1 h and then stirred for 1 h to enhance the physical mixing between the two components. After that, the solid was collected by centrifugation and dried at 80 °C. Next, the mixture was sealed in the vacuum quartz ampoule. The ampoule was heated to 600 °C for 2 h (5 °C $min^{-1}$) in a furnace, followed by cooling to 300 °C (1 °C $min^{-1}$) and then slowly to room temperature (0.1 °C $min^{-1}$). The sample was collected and washed with carbon disulfide solution and water/ethanol solution several times to remove the byproducts. Finally, the product was obtained and readily usable after drying at 50 °C. Pristine crystalline red P was prepared with the same experimental condition, but in the absence of GO.

### C. Structural characterization and measurement of charge carrier dynamics

The morphology of the as-prepared samples was characterized by scanning electron microscopy (SEM, QF400), transmission electron microscopy (TEM, Tecnai TS12), and high-resolution transmission electron microscopy (HRTEM, Philips CM-120). X-ray powder diffraction (XRD) patterns of samples were collected with a Rigaku SmartLab x-ray diffractometer using Cu Kα irradiation in the $2\theta$ range from 10° to 60°. Raman spectra of samples were recorded on a Renishaw RM3000 Micro-Raman system with 532 nm laser excitation. UV–vis spectra of samples were recorded on Varian Cary100 scan spectrophotometers. X-ray photoelectron spectroscopy (XPS) of the samples was conducted on a Thermo ESCALAB 250Xi spectrometer.

The femtosecond TA (fs-TA) experiment was performed on an automated data acquisition transient absorption spectrometer (Ultrafast, Helios) equipped with a commercial femtosecond Ti/sapphire regenerative amplifier laser system (Mai Tai, Spitfire-Pro, Spectra Physics Company). The amplifier was seeded with the laser output from the oscillator (Maitai, Spectra Physics) and generated 120 fs pulses at 800 nm with a repetition rate of 1 kHz and an average power of 2.6 W. Approximately 95% of the amplified 800 nm output (Spitfire) was used to generate the 400 nm pump laser on the second harmonic generator BBO crystal, while the remaining 5% of the amplified 800 nm output was focused on a Ti/sapphire crystal to generate a white-light continuum spectrum (420 nm–780 nm) as a probe laser. The pump and probe beams were focused onto the magnetically stirred sample cell (2 mm optical path length). The instrument response function of this system was determined to be 150 fs.

The Vienna *Ab initio* Simulation Package (VASP) was used by applying the projector-augmented-wave method with the Perdew–Burke–Ernzerhof generalized gradient approximation (GGA) functional. The electronic convergence limit was set to $1 \times 10^{-4}$ eV. The van der Waals d2 correction was taken into account. Optimization of atomic coordinates was considered to be converged if the Hellmann–Feynman force was smaller than $5 \times 10^{-2}$ eV $Å^{-1}$. Bulk crystalline red P and slabs of (−201), (−340), (−101), (−401), and (−301) surfaces were constructed. Each slab consists of 84 phosphorus atoms. All the atoms were relaxed during optimization. The vacuum region is about 15 Å in height. We applied the Monkhorst–Pack scheme 3 × 3 × 1 for k-point selection and resulted in five irreducible k-points.

### D. Photoelectrochemical (PEC) measurements and photocatalytic hydrogen evolution experiments

All photoelectrochemical (PEC) and electrochemical measurements were carried out on a CHI 760D potentiostat/galvanostat in a standard three-electrode configuration. The Ag/AgCl and Pt electrodes were used as the reference and counter electrodes, respectively, while the electrolyte was composed of 0.1M $Na_2SO_4$ aqueous solution. Irradiation was provided through a 300 W Xenon lamp (PLS-SXE300). Photoelectrodes were prepared by dropcasting 2 mg of sample onto the fluorine doped tin oxide (FTO) glass substrate (1.5 × 1.5 $cm^2$) and dried in an oven at 160 °C for 1 h. Linear sweep voltammetry (LSV) was performed with a scan rate of 1 mV $s^{-1}$ with and without the addition of 0.01M $H_2O_2$ in the electrolyte. The charge transfer efficiency ($\eta_{transfer}$) was calculated according to the following equation:

$$\eta_{transfer(\%)} = \frac{J(H_2O,\ light) - J(H_2O,\ dark)}{J(H_2O_2,\ light) - J(H_2O_2,\ dark)} \times 100\%, \quad (1)$$

where $J$ is the measured photocurrent in the presence or absence of $H_2O_2$ under dark or photoirradiation. The key assumption for calculating $\eta_{transfer}$ is that the oxidation kinetics of $H_2O_2$ is very fast and the charge transfer efficiency on both of the red P and red P/RGO electrodes is referenced as 100%.[28,29] Therefore, the ratio of photocurrent density measured in $H_2O$ and $H_2O_2$ gives the charge transfer efficiency for $H_2O$. The amperometric photocurrent was measured at 0.5 V vs Ag/AgCl.

The photocatalytic hydrogen evolution experiments were carried out on a Pyrex reaction cell connected to a closed gas circulation and evacuation system. Visible-light irradiation was provided through the 300 W Xenon lamp fitted with a L40 cut-off filter. Samples (20 mg) were dispersed in 50 ml of aqueous solution containing 10 vol. % triethanolamine as the sacrificial holes scavenger. Additional 3 wt. % Pt cocatalyst was *in situ* photodeposited on the surface of photocatalysts. The amount of hydrogen generated from the photocatalytic reaction was measured on a Techcomp GC 7900 gas chromatograph equipped with a thermal conductive detector (TCD) detector. High purity argon gas was used as a carrier gas. The apparent quantum yield (AQY) was calculated from AQY = (2 × number of evolved hydrogen molecules)/(number of incident photons) × 100%.

## III. RESULTS AND DISCUSSION

The crystalline red P and red P/RGO composites were prepared using a vacuum-sealed ampoule chemical vapor deposition (CVD) method, as depicted in Fig. 1(a). Amorphous red P and graphene oxide (GO) were used as the starting materials. Sublimation of bulky amorphous P [>1 $\mu$m, Fig. S1(a) of the supplementary material] took place during the heating of the sample to 600 °C ($T_{sublime}$ ~420 °C), while the two-dimensional GO nanosheets would thermally reduce under vacuum to form RGO [Fig. S1(b) of the supplementary material]. Subsequent cooling of the ampoule resulted in the condensation and homogeneous deposition of crystalline P nanoparticles on the large surface area RGO sheets. The formed crystalline P were of <30 nm, whether in their pristine form [Figs. 1(b) and 1(c)] or supported on RGO [Figs. 1(e) and 1(f)]. In addition, both samples reveal clear lattice fringes with interplanar distances, e.g., 0.26 Å, 0.30 Å, 0.41 Å, 0.51 Å, and 0.61 Å, which correspond to [3 4 0], [4 0 1], [3 0 1], [2 0 1], and [1 0 1], respectively [Figs. 1(d) and 1(g), and Fig. S2 of the supplementary material]. X-ray diffraction (XRD) shows the same set characteristic peaks of crystalline fibrous phase red P in both pristine and RGO-supported samples [Fig. 2(a)].[4,5,13] An additional peak at $2\theta$ = 26.3° was observed in the former,

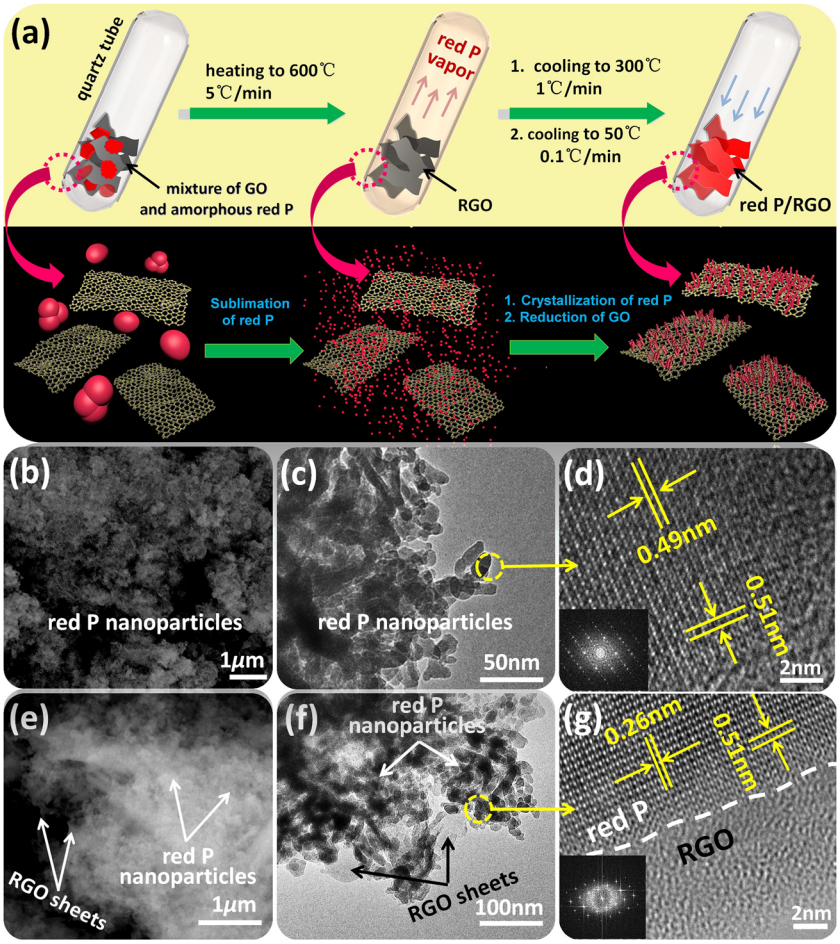


**FIG. 1**. (a) Synthetic procedure of samples by one-step, vacuum-sealed ampoule CVD method. Also shown are the (b) SEM, (c) TEM and (d) HRTEM of the crystalline red P, and the respective images (e)–(g) of the as-prepared red P/RGO.

which can be traced to the diffraction of the [0 0 2] plane of the RGO.[29–31]

The Raman spectrum of the red P/RGO composite in Fig. 2(b) reveals the characteristic peaks for the red P below 500 $cm^{-1}$ and that of graphene at 1347 $cm^{-1}$ (D band) and 1576 $cm^{-1}$ (G band). Compared with the bare GO ($I_D/I_G$ = 0.92), the red P/RGO shows an increased $I_D/I_G$ = 1.22, indicating the reduction of GO to RGO. From x-ray photoelectron spectroscopy (XPS), the extent of reduction was quantified to be 88% based on the ratio of the integrated area of the C–C bond to that of total C bonds, i.e., C–C and C–O [Fig. 2(c)]. As shown from the high-resolution P $2p_{3/2}$ spectra of red P [Fig. 2(d)], the two binding energy peaks of 130.1 eV and 130.9 eV can be attributed to the surface elemental P (i.e., P–P bond) as well as that bonded with carbon impurities, i.e., through the adsorption of ubiquitous volatile organic carbons in the ambient. In the red P/RGO sample, the surface amount of elemental P was drastically reduced as accompanied by the formation of new P–O–C bonds (binding energy = 131.8 eV) arising from the chemical attachment of red P to RGO.[32–34]

To establish the band structure of the red P, information from different measurements was collated and hereby presented as Fig. 3. Figure 3(a) shows the UV–vis diffuse-reflectance spectra of the red P and red P/RGO, plotted in Kubelka–Munk absorbance. The elevated baseline in the latter sample is typical of the broad absorbance of the $\pi$ electron in RGO.[35] The optical bandgap of the crystalline red P was estimated from the Tauc plot to be 1.75 eV [see Fig. 3(b)]. The p-type characteristic of the red P was confirmed by the Mott–Schottky plots with a negative slope from which the extension of the linear portion to the abscissa yielded the flatband potential of +0.77 V vs NHE [Fig. 3(c)]. Figure 3(d) shows the valence band (VB) spectra from which the energy gap between the flatband potential and the VB edge was readily deduced to be 0.71 eV. Combining all the information above, the VB and conduction band (CB) edge potentials could be calculated to be +1.48 and −0.27 V vs NHE, respectively [Fig. 3(e)].

To evaluate the charge transfer efficiencies of the red P and red P/RGO, anodic linear sweep voltammetry (LSV) was carried out in the presence and absence of $H_2O_2$ sacrificial hole scavenger

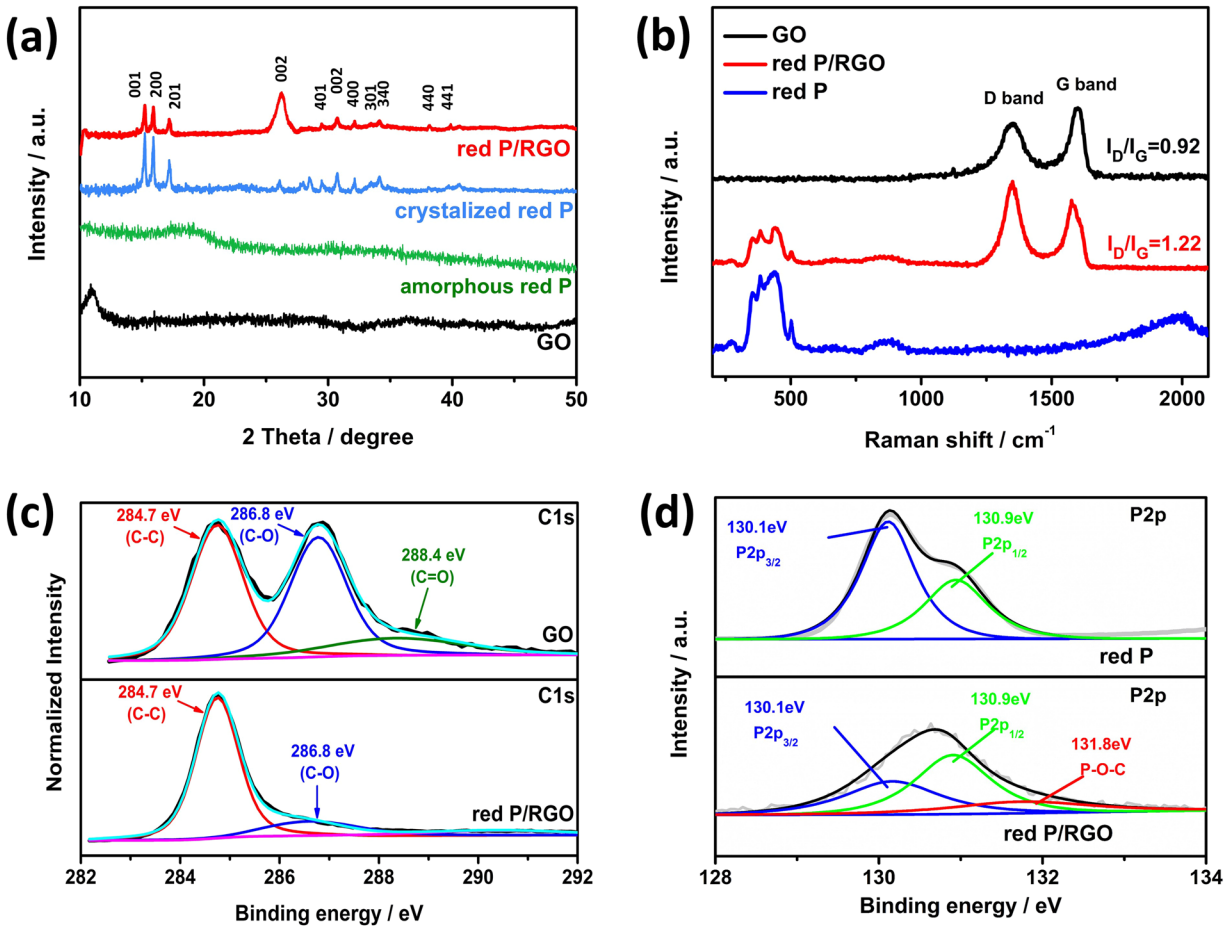


**FIG. 2**. (a) XRD spectra, (b) Raman spectra, (c) C1s XPS, and (d) P2p XPS of the samples.

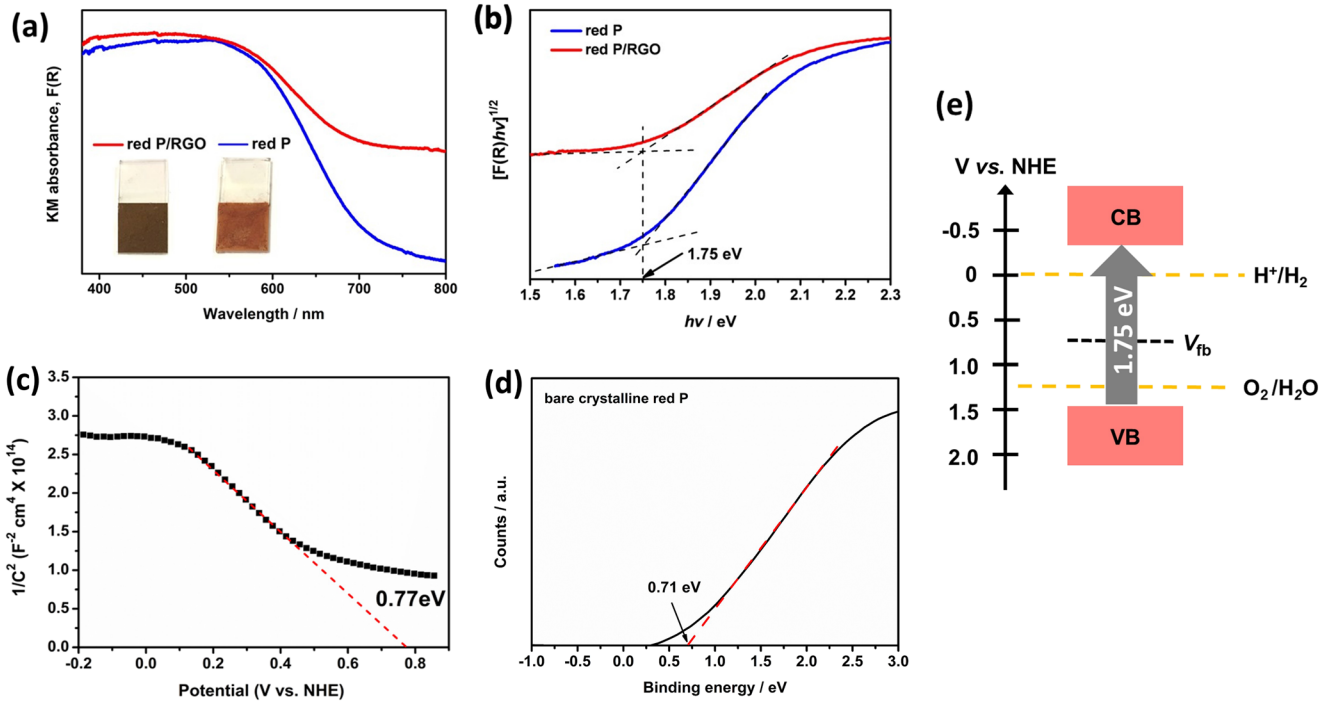


**FIG. 3**. (a) Kubelka–Munk absorbance spectra of the red P and red P/RGO samples as well as the photographs of the respective samples coated on FTO glass, and (b) the corresponding Tauc plot, as well as (c) the Mott–Schottky plot of the red P, (d) the valence band XPS, and (e) the deduced band structure of the crystalline red P.

[Fig. 4(a)]. The relative photocurrent in both cases can be taken as a measure of charge transfer efficiencies [$\eta_{transfer}$, Eq. (1)].[28,29] As shown in Fig. 4(b), $\eta_{transfer}$ of pristine red P remains relatively low even with increasing band bending at higher potentials. The results suggest severe trapping of photocharges at the TS, potentially leading to an extensive charge recombination. This effect will be verified by TA decay kinetics below. By comparison, the red P/RGO shows up to four times greater in $\eta_{transfer}$, demonstrating the efficacy of the RGO in circumventing the deep trapping of photoelectrons in red P as promoted by the interfacial charge transport.[35] Since the trapping at TS is no longer the limiting factor, the surface transfer process was significantly increased with increasing potential, reaching up to $\eta_{transfer}$ = 83% at 0.8 V vs NHE. Figure 4(c) shows the amperometric curves of the samples under alternating visible-light on–off irradiation. Besides the higher photocurrent of red P/RGO compared to the pristine red P, note the reproducible photoresponses measured for both samples under the repeated on–off cycles that indicate the high photostability of the samples.

The photocatalytic hydrogen evolution (PHE) of the aqueous suspensions of red P and red P/RGO was evaluated under visible-light irradiation (Fig. 5). As expected, a much higher PHE rate of

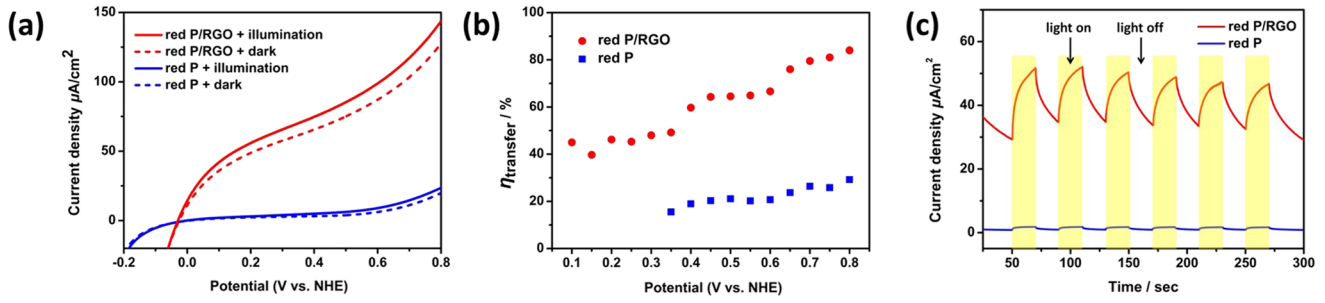


**FIG. 4**. (a) Linear sweep voltammetry (LSV) of red P and red P/RGO in the presence or absence of 0.01 M $H_2O_2$ and (b) the corresponding charge transfer efficiency ($\eta_{transfer}$). (c) Amperometric photocurrent responses of red P and red P/RGO measured under light chopping (periodic on–off) mode.

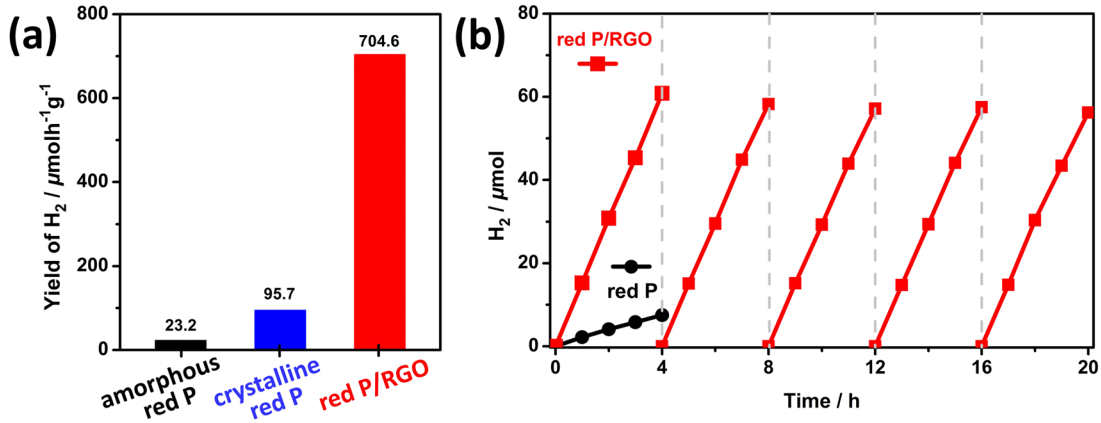


**FIG. 5**. (a) The photocatalytic hydrogen evolution rates on bare amorphous red P, bare crystalline red P, and red P/RGO under visible-light irradiation, and (b) cycling assessment of the hydrogen evolution reaction on red P/RGO under visible-light irradiation.

705 $\mu$mol $h^{-1}$ $g^{-1}$ was measured for the red P/RGO, which is sevenfold higher than that of pristine red P (95.7 $\mu$mol $h^{-1}$ $g^{-1}$). By comparison, amorphous red P is only mildly active with the PHE rate of 23.2 $\mu$mol $h^{-1}$ $g^{-1}$ [Fig. 5(a)]. In terms of apparent quantum yield (AQY), the red P/RGO gives AQY = 3.1% at 650 nm, which is nearly threefold of the bare red P (1.12%), comparable to the composite black P reported by Zhu and co-workers.[36,37] Importantly, the sustained PHE over 20 h of continuous irradiation during the recycling experiment corroborated the earlier observation on the high stability of the red P/RGO sample [Fig. 5(b)].

The analysis of the photocharge carrier dynamics of the red P was carried out using fs-TA spectroscopy. Upon photoexcitation with 400 nm laser pulse (50 fs), a broad band of 400–800 nm with maxima at ~600 nm belonging the absorption of the excited states (ESs) could be measured [Fig. 6(a)]. The absorbance gradually decayed over the next few hundred ps, followed by the slow ns bleaching of the ground state (GS) and a later stage recovery. The trend is consistent with the earlier measurements carried out by others on black P.[38,39] Figure 6(b) shows the higher resolution TA decay kinetics of the red P, where a rather consistent kinetics trend was observed at different probe wavelengths. In other words, the transient states were likely to exist over a relatively broad energetic profile. From the TA kinetics, the generation of ES in red P peaked at 5 ps delay, followed by a two-component exponential decay on the ps time scale. The time constant (as shown in Table S2 of the supplementary material) for the fast decay component ($\tau_1$ = 16 ps, 38%) is attributed to the charge trapping process (ES to TS), while the slower but dominant decay component ($\tau_2$ = 202 ps, 62%) is due to the bulk recombination (ES to the GS).[27] The bleaching of GS, which reflects a higher number of holes in the valence band compared with the ES electrons (with the remaining portion of the photoelectrons in TS), can be evident from 200 ps up to a few ns. Scheme 1(a) depicts the overall process of charge carrier dynamics. To prove that the TS electrons are the limiting factor in the photocatalytic process, the TA kinetics of red P were measured under three conditions: (1) aerated aqueous suspension, i.e., in the presence of $O_2$ as an efficient electron scavenger, (2) deaerated aqueous suspension, i.e., $H^+$ as an electron scavenger, and (3) acetonitrile suspension, i.e., without electron and hole scavengers. As shown in Fig. 6(c), the TA decay curves in (1) and (2) overlapped one another since the overall surface transfer process is limited by the electron trapping at TS. By comparison, a slightly higher extent of GS bleaching could be measured in (3) compared to the other two samples due to the higher ratio of valence band holes to ES electrons, or in other words, a higher fraction of electrons in the TS, as a result of the higher density of charge accumulation in the absence of redox reactions.

To gain further insights into the origin of the TS in red P, we performed band structure calculation by density functional calculations. As shown in Fig. 7(a), a clear bandgap of 1.65 eV, which is nearly consistent with the experimental results, can be observed from the band diagram of the bulk crystalline red P. There is hardly any TS between the conduction and valence bands in the bulk crystalline red P. However, when analyzed as facet-specific slabs including (−2 0 1), (−3 4 0), (−1 0 1), and (−3 0 1), a series of TS can be found within the forbidden band [Figs. 7(b)–7(e)]. These intrinsic TS, when taken together, spread over the wide energy range, from as little as 1.65 eV for (−1 0 1) facets to 0.75 eV for (−3 0 1) facets. Because these TSs are situated at more than 50 meV below the conduction band edge, they may not be readily detrapped by the ambient thermal energy, $k_BT$.[40]

Figure 8(a) shows the TA of red P/RGO, which is similar to the absorbance spectra of red P, except for the much faster ES decay and absence of GS bleaching. Figure 8(b) compares the intensity-normalized decay kinetics of the red P and red P/RGO. While the kinetics of ES generation were similar for both samples (see Table S1 of the supplementary material), i.e., peaking within 5 ps, the latter is characterized by a much faster first component decay ($\tau_1$ = 3.1 ps, 75%) that is at the same time more dominant compared with the red P ($\tau_1$ = 16 ps, 38%). The much faster time constant points to a new decay process, which, in this case, is attributed to the interfacial transport of the ES electrons from the red P conduction band to RGO. This is further supported by the absence of GS bleaching that reflects the balance of photoelectrons and holes in the

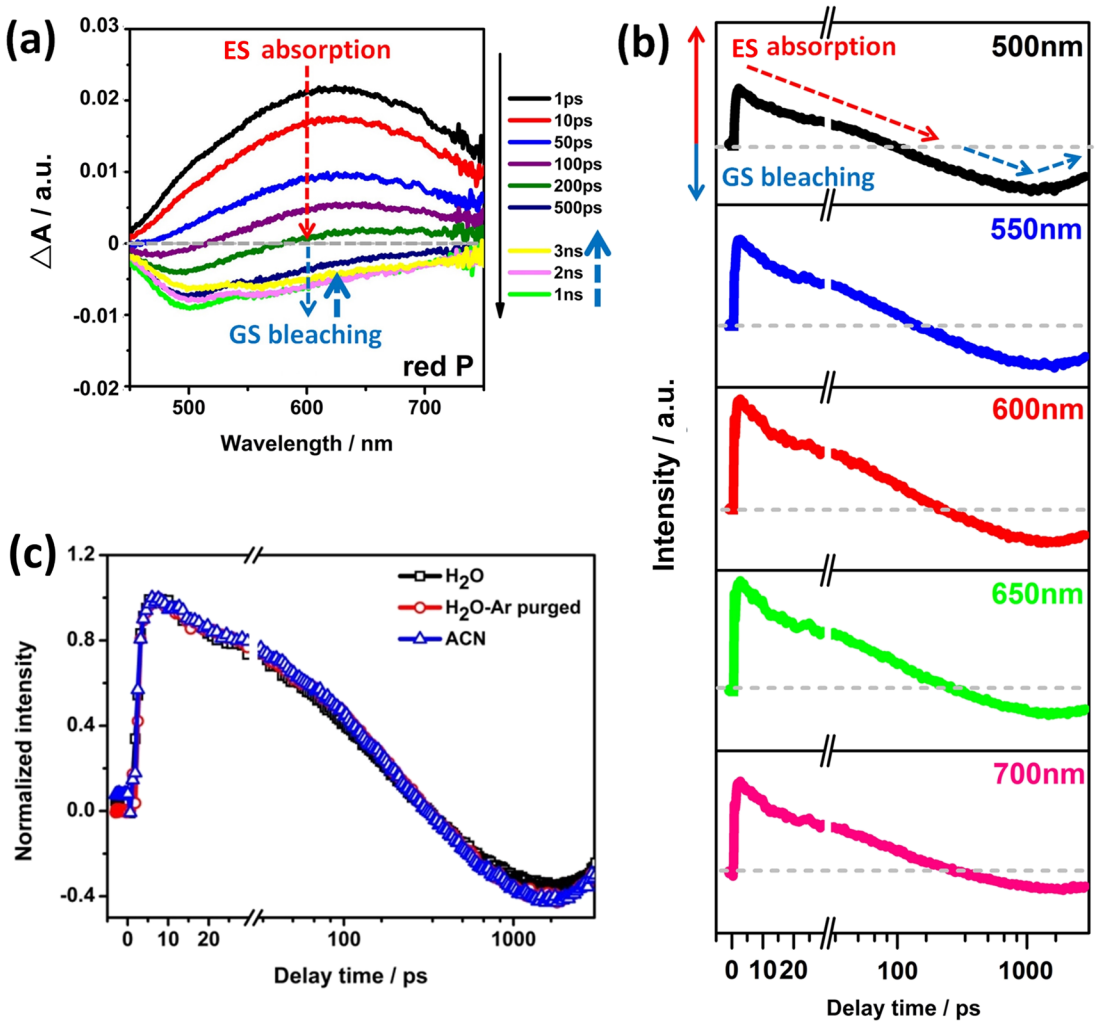


**FIG. 6**. (a) Absorbance spectra of red P collected at various time delays, and (b) the fs-TA decay kinetic curves of red P probed at 500, 550, 600, 650, and 700 nm. (c) The fs-TA decay kinetics (probed at 600 nm) of red P measured in an aqueous suspension with and without argon purge and in acetonitrile (ACN).

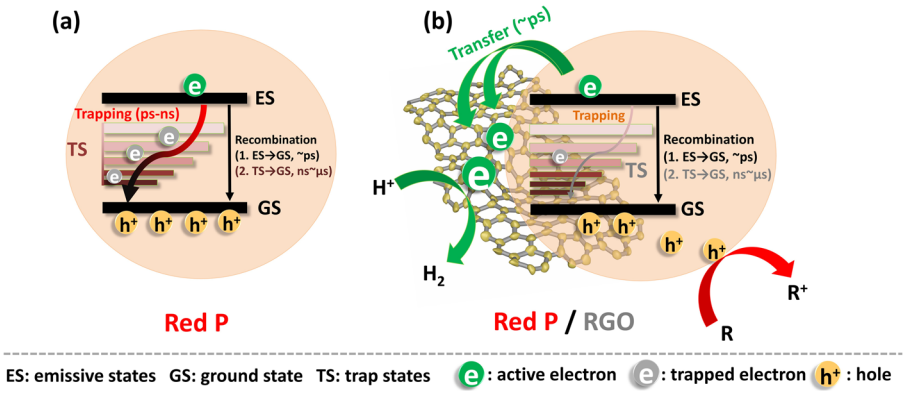


**SCHEME 1**. Proposed mechanism of charge dynamics in (a) red P and (b) red P/RGO upon photoexcitation.

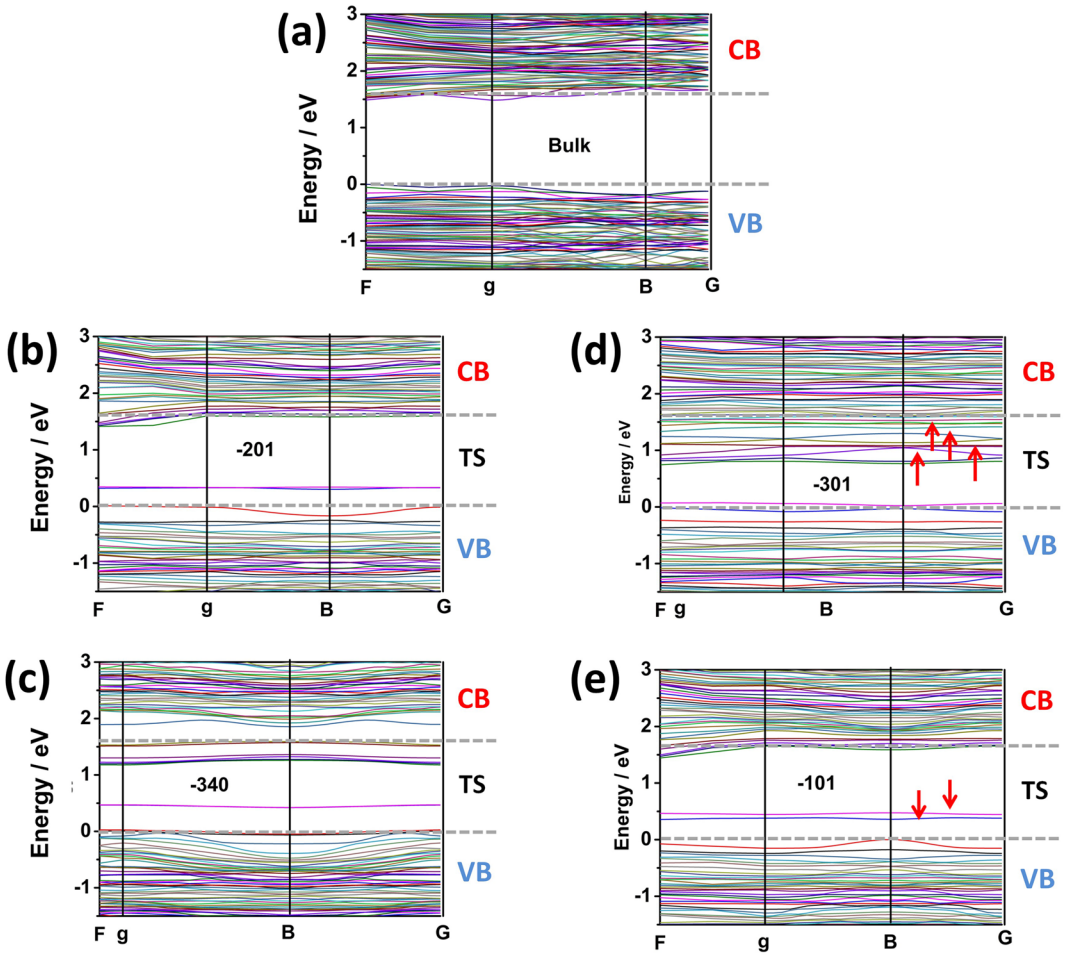


**FIG. 7**. DFT-calculated band structure of (a) bulk red P as well as that of the (b) (−201), (c) (−340), (d) (−301), and (e) (−101) surfaces.

conduction and valence bands, respectively, or in other words, a minimal amount of electrons in the TS [Scheme 1(b)]. In fact, the ultrafast interfacial electron transport and further surface transfer on RGO dominated as the primary process, inferring an equally fast surface hole transfer process, at the expense of the slower component decay associated with the bulk recombination ($\tau_2$ = 210 ps, 25%). To recap, photoexcitation of the red P led to the severe trapping of photoelectrons at TS, resulting in accumulated photoholes

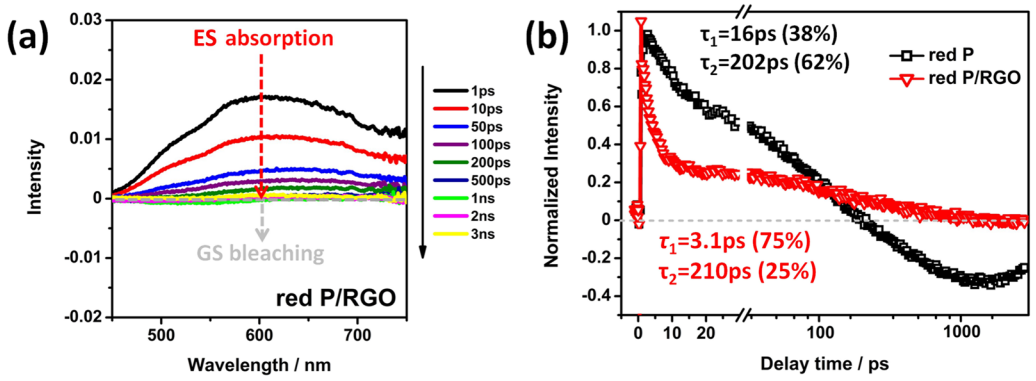


**FIG. 8**. (a) Absorbance spectra of red P/RGO collected at various time delays, and (b) the fs-TA decay kinetics of red P and red P/RGO probed at 600 nm.

on the valence band (to preserve charge neutrality). These trapped photoelectrons at TS, which take up to a few ns to recombine, are generally redox inactive in the current studies. Coupling with RGO effectively circumvented the trapping of ES electrons at TS by favoring the effective interfacial transfer to RGO. This makes available the photoelectrons on RGO for surface reduction reaction, allowing an equally fast surface photoholes transfer. The rate of photoelectron transfer to RGO appears to match that of the surface hole transfer to minimize the GS bleaching. The TA analysis consolidated the photoelectrochemical measurements on the enhanced charge transfer efficiencies as well as the enhanced photocatalytic activity of the red P/RGO composite. Given the relatively short lifetime (~1 ns) of the active photocharges of the red P even after interfacing with RGO, likely limited by the intrinsically slow charge mobility of the former material, we envision much higher photocatalytic efficiencies by overcoming this factor alone.

## IV. CONCLUSIONS

The work showcases the ampoule CVD-synthesis of a highly active red P/RGO composite photocatalyst for stable and recyclable hydrogen production under visible-light irradiation. While the as-synthesized pristine red P (fibrous phase) was highly crystalline, there were intrinsic deep traps associated with the different crystal facets. The severe charge trapping at these deep traps essentially limited the overall surface transfer and hence the photocatalytic activity of the red P. As confirmed by ultrafast TA spectroscopy, the coupling of red P with RGO provided a highly effective interfacial charge transport route that essentially circumvented the charge trappings. This resulted in a drastic improvement in the hydrogen production rate. The findings from this work can serve as an important platform for the research community to introduce other strategies for mitigating the effects of charge trappings in red P, e.g., the addition of suitable cocatalysts, design of reactive facets with minimum deep traps, and improving the bulk charge mobility through doping.

## SUPPLEMENTARY MATERIAL

See the supplementary material for the experimental section for the purification of commercial red P and the preparation of GO, the SEM and HRTEM images of the samples, and the table for the exponential fits for the fs-TA decay of red P and the red P/RGO composite.

## AUTHORS' CONTRIBUTIONS

L.J. and R.Z. contributed equally to this work.

## ACKNOWLEDGMENTS

This work was partially supported by the Research Grants Council of Hong Kong (Project No. 14305417). This work was also supported by the National Natural Science Foundation of China (Grant No. 51902008) and Research funds for high-level talents (Grant No. 005000514119046). Partial support from the Grants Committee Areas of Excellence Scheme (AoE/P-03/08) and the Special Equipment Grant (Grant No. SEG HKU/07) is acknowledged. The University of Hong Kong Development Fund 2013–2014 project "New Ultrafast Spectroscopy Experiments for Shared Facilities" and the Faculty of Science RAE Improvement Fund are also gratefully acknowledged. The theoretical calculation was supported by the National Supercomputer Center in Guangzhou and National Supercomputing Center in Shenzhen (Shenzhen Cloud Computing Center). W.Y.T. acknowledges the support from the Research Grants Council of Hong Kong (Project No. 11337116) and the Australian Research Council through the Discovery Grant (No. DP200102121).

## DATA AVAILABILITY

The data that support the findings of this study are available from the corresponding author upon reasonable request.

## REFERENCES

[1] W.-J. Ong, L.-L. Tan, Y. H. Ng, S.-T. Yong, and S.-P. Chai, Chem. Rev. **116**, 7159 (2016).
[2] P. Yang, H. Ou, Y. Fang, and X. Wang, Angew. Chem., Int. Ed. **56**, 3992 (2017).
[3] K. L. Corp and C. W. Schlenker, J. Am. Chem. Soc. **139**, 7904 (2017).
[4] Z. Hu, L. Yuan, Z. Liu, Z. Shen, and J. C. Yu, Angew. Chem. **55**, 9580 (2016).
[5] Z. Hu, Z. Shen, and J. C. Yu, Green Chem. **19**, 588 (2017).
[6] F. Wang, W. K. H. Ng, J. C. Yu, H. Zhu, C. Li, L. Zhang, Z. Liu, and Q. Li, Appl. Catal., B **111-112**, 409 (2012).
[7] Z. Shen, S. Sun, W. Wang, J. Liu, Z. Liu, and J. C. Yu, J. Mater. Chem. A **3**, 3285 (2015).
[8] F. Wang, C. Li, Y. Li, and J. C. Yu, Appl. Catal., B **119-120**, 267 (2012).
[9] Z. Shen, Z. Hu, W. Wang, S.-F. Lee, D. K. Chan, Y. Li, T. Gu, and J. C. Yu, Nanoscale **6**, 14163 (2014).
[10] L. Jing, R. Zhu, D. L. Phillips, and J. C. Yu, Adv. Funct. Mater. **27**, 1703484 (2017).
[11] F. Bachhuber, J. von Appen, R. Dronskowski, P. Schmidt, T. Nilges, A. Pfitzner, and R. Weihrich, Angew. Chem., Int. Ed. **53**, 11629 (2014).
[12] O. Osters, T. Nilges, F. Bachhuber, F. Pielnhofer, R. Weihrich, M. Schöneich, and P. Schmidt, Angew. Chem., Int. Ed. **51**, 2994 (2012).
[13] M. Ruck, D. Hoppe, B. Wahl, P. Simon, Y. Wang, and G. Seifert, Angew. Chem., Int. Ed. **44**, 7616 (2005).
[14] A. Pfitzner, M. F. Bräu, J. Zweck, G. Brunklaus, and H. Eckert, Angew. Chem., Int. Ed. **43**, 4228 (2004).
[15] A. Pfitzner, Angew. Chem., Int. Ed. **45**, 699 (2006).
[16] D. Xia, Z. Shen, G. Huang, W. Wang, J. C. Yu, and P. K. Wong, Environ. Sci. Technol. **49**, 6264 (2015).
[17] J. B. Smith, D. Hagaman, D. DiGuiseppi, R. Schweitzer-Stenner, and H.-F. Ji, Angew. Chem., Int. Ed. **55**, 11829 (2016).
[18] W.-C. Chang, K.-W. Tseng, and H.-Y. Tuan, Nano Lett. **17**, 1240 (2017).
[19] S. A. Ansari, M. O. Ansari, and M. H. Cho, Sci. Rep. **6**, 27713 (2016).
[20] L. Jiang, X. Yuan, G. Zeng, X. Chen, Z. Wu, J. Liang, J. Zhang, H. Wang, and H. Wang, ACS Sustainable Chem. Eng. **5**, 5831 (2017).
[21] K. Wang, Q. Li, B. Liu, B. Cheng, W. Ho, and J. Yu, Appl. Catal., B **176-177**, 44 (2015).
[22] J. Ran, T. Y. Ma, G. Gao, X.-W. Du, and S. Z. Qiao, Energy Environ. Sci. **8**, 3708 (2015).
[23] V. S. Chirvony, S. González-Carrero, I. Suárez, R. E. Galian, M. Sessolo, H. J. Bolink, J. P. Martínez-Pastor, and J. Pérez-Prieto, J. Phys. Chem. C **121**, 13381 (2017).
[24] H. Kasap, C. A. Caputo, B. C. Martindale, R. Godin, V. W.-h. Lau, B. V. Lotsch, J. R. Durrant, and E. Reisner, J. Am. Chem. Soc. **138**, 9183 (2016).

[25]J. J. Walsh, C. Jiang, J. Tang, and A. J. Cowan, Phys. Chem. Chem. Phys. **18**, 24825 (2016).
[26]R. Kuriki, H. Matsunaga, T. Nakashima, K. Wada, A. Yamakata, O. Ishitani, and K. Maeda, J. Am. Chem. Soc. **138**, 5159 (2016).
[27]R. Godin, Y. Wang, M. A. Zwijnenburg, J. Tang, and J. R. Durrant, J. Am. Chem. Soc. **139**, 5216 (2017).
[28]I. S. Cho, C. H. Lee, Y. Feng, M. Logar, P. M. Rao, L. Cai, D. R. Kim, R. Sinclair, and X. Zheng, Nat. Commun. **4**, 1723 (2013).
[29]L. Jing, H. L. Tan, R. Amal, Y. H. Ng, and K.-N. Sun, J. Mater. Chem. A **3**, 15675 (2015).
[30]H. L. Tan, X. Wen, R. Amal, and Y. H. Ng, J. Phys. Chem. Lett. **7**, 1400 (2016).
[31]H. L. Tan, H. A. Tahini, X. Wen, R. J. Wong, X. Tan, A. Iwase, A. Kudo, R. Amal, S. C. Smith, and Y. H. Ng, Small **12**, 5295 (2016).
[32]Y. Zhao, S. Huang, M. Xia, S. Rehman, S. Mu, Z. Kou, Z. Zhang, Z. Chen, F. Gao, and Y. Hou, Nano Energy **28**, 346 (2016).
[33]Y. Liu, A. Zhang, C. Shen, Q. Liu, X. Cao, Y. Ma, L. Chen, C. Lau, T.-C. Chen, F. Wei, and C. Zhou, ACS Nano **11**, 5530 (2017).
[34]J. Sun, H.-W. Lee, M. Pasta, Y. Sun, W. Liu, Y. Li, H. R. Lee, N. Liu, and Y. Cui, Energy Storage Mater. **4**, 130 (2016).
[35]H. Yang, S. V. Kershaw, Y. Wang, X. Gong, S. Kalytchuk, A. L. Rogach, and W. Y. Teoh, J. Phys. Chem. C **117**, 20406 (2013).
[36]M. Zhu, C. Zhai, M. Fujitsuka, and T. Majima, Appl. Catal., B **221**, 645 (2018).
[37]M. Zhu, Z. Sun, M. Fujitsuka, and T. Majima, Angew. Chem., Int. Ed. **57**, 2160 (2018).
[38]L. Chen, C. Zhang, L. Li, H. Wu, X. Wang, S. Yan, Y. Shi, and M. Xiao, J. Phys. Chem. C **121**, 12972 (2017).
[39]L. Bai, X. Wang, S. Tang, Y. Kang, J. Wang, Y. Yu, Z.-K. Zhou, C. Ma, X. Zhang, J. Jiang, P. K. Chu, and X.-F. Yu, Adv. Mater. **30**, 1803641 (2018).
[40]M. R. Hoffmann, S. T. Martin, W. Choi, and D. W. Bahnemann, Chem. Rev. **95**, 69 (1995).